Oxidation of ultralene and paraffin due to radiation damage after exposure to soft X-rays probed by FTIR microspectroscopy and X-ray fluorescence

Diana E. Bedolla,[a,b]* Giovanni Birarda,[a] Sabina Giannotta,[c] Valentina Faoro,[c] Alberto Cescato,[c] Lisa Vaccari[a] and Alessandra Gianoncelli[a]

[a]Elettra-Sincrotrone Trieste, S.S. 14 Km 163.5 in Area Science Park, Basovizza, TS 34149, Italy, [b]Area Science Park, Padriciano 99, Padriciano, TS 34149, Italy, and [c]Laboratori Riuniti – Synlab, Via delle Mura 2, Trieste, TS 34121, Italy. *Correspondence e-mail: diana.bedolla@elettra.eu
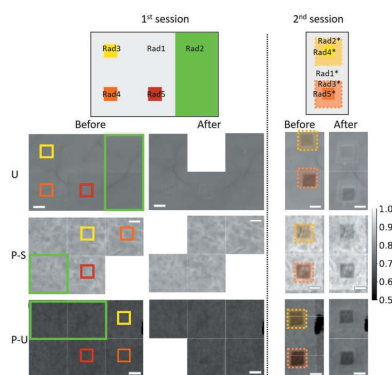
Radiation damage upon soft X-ray exposure is an important issue to be considered in soft X-ray microscopy. The work presented here is part of a more extended study on the topic and focuses on the effects of soft X-rays on paraffin, a common embedding medium for soft-tissues, and on ultralene and Si_3N_4 windows as sample supports. Our studies suggest that the sample environment indeed plays an important role in the radiation damage process and therefore should be carefully taken into account for the analysis and interpretation of new data. The radiation damage effects were followed over time using a combination of Fourier transform infrared (FTIR) microspectroscopy and X-ray fluorescence (XRF), and it was demonstrated that, for higher doses, an oxidation of both embedding medium and ultralene substrate takes place after the irradiated sample is exposed to air. This oxidation is reflected in a clear increase of C=O and O—H infrared bands and on the XRF oxygen maps, correlated with a decrease of the aliphatic infrared signal. The results also show that the oxidation process may affect quantitative evaluation of light element concentrations.

1. Introduction

Soft X-ray microscopy is becoming a very powerful tool for the analysis of samples at sub-micrometre length scales, and especially biological samples. In particular, this technique provides morphological information and, when combined with X-ray fluorescence, also information on the chemical content and elemental distribution. One of the main issues that remains to be clarified is how invasive the technique is from a radiation damage point of view. Even though this topic has attracted the attention of several microscopy groups in the past decades (Beetz & Jacobsen, 2003; Wang et al., 2009; Lombi et al., 2011; Kosior et al., 2012; Jones et al., 2017, 2020; Howells et al., 2009) and new studies have appeared, the available literature, especially regarding soft X-rays, still remains sparse and not comprehensive. Most groups (Beetz & Jacobsen, 2003; Wang et al., 2009; Lombi et al., 2011; Kosior et al., 2012; Jones et al., 2017, 2020; Howells et al., 2009) have been mainly investigating the entity of radiation damage using the same X-ray techniques utilized to induce the damage, whereas our group has been assessing it also by means of non-destructive techniques such as infrared microspectroscopy and atomic force microscopy (AFM) (Gianoncelli et al., 2015; Bedolla et al., 2018). FTIR spectroscopy provides vibrational information on the sample, whereas AFM provides morphological/topographical information. Our team has been investigating this issue over the past few years as well, starting by

evaluating the effects of soft X-rays on cells and tissues by considering two typical biological sample preparations: fixed cells (Gianoncelli *et al.*, 2015) and paraffin embedded tissues (Bedolla *et al.*, 2018). Indeed, the sample preparation may not only affect the chemistry and/or morphology of the sample itself but also it may play a role in the radiation damage process. In particular, our last study (Bedolla *et al.*, 2018) suggests that both embedding medium and substrate may influence the extent of the radiation damage effects, showing that some sample preparation protocols seem to be more resistant than others to radiation damage.

The current work focuses on the substrate, by tackling the behaviour under soft X-rays of histological paraffin deposited onto two typical sample supports, ultralene film and Si_3N_4 membranes, by decoupling the effects of each of the components (substrate and embedding medium) from the tissue itself, allowing for a better understanding of the radiation damage process. Ultralene is among the most used sample supports for transmission X-ray microscopy analyses, especially for tissue samples. To be measured, thick samples, like organs, need to be sliced by a microtome; this sample preparation procedure may also require sample embedding in suitable matrices. Paraffin embedding is one of the most common protocols for sectioning human or animal tissues, conventionally used for histopathology studies and often also for X-ray microscopy investigations (Paunesku *et al.*, 2012; Takahashi *et al.*, 2010; Chwiej *et al.*, 2005; Pascolo *et al.*, 2013; Merolle, Ragazzi *et al.*, 2018; Pickler *et al.*, 2019). However, it has been recently demonstrated that both ultralene and paraffin on ultralene undergo degradation and consequent oxidation when exposed to soft X-rays (Bedolla *et al.*, 2018).

Another important aspect to be considered is that the radiation damage phenomenon is determined by the contribution of various processes (Sanishvili *et al.*, 2011), being the result of a primary and a secondary damage, the first initiated by the ionizing radiation and the second induced by secondary ionization events and reactive radicals (Carugo & Carugo, 2005). The primary effect is mainly dose- and sample preparation-dependent, whereas the second effect seems to be mainly time- and environment-dependent. In fact, during our previous study (Bedolla *et al.*, 2018) we observed that, after removing the sample from the vacuum environment of the soft X-ray microscope, the damage might still progress, showing a trend with time and becoming the motivation for this work.

Therefore, the current work explores not only the behaviour of paraffin on two different samples supports (ultralene film and Si_3N_4 membrane), but also the evolution of the damage with time, by investigating the samples just after removal from the vacuum atmosphere, and after one hour, one day and one week of air exposure. Also, in order to decouple the contribution of the ultralene from the paraffin, ultralene alone was exposed and characterized in the same way as well as paraffin on an Si_3N_4 membrane support. Additionally, X-ray fluorescence (XRF) mapping was re-applied on the already exposed samples, after FTIR measurements performed in air, to investigate possible changes in light element contents. The results shown in the present work

provide further knowledge on the understanding of radiation damage, highlighting different contributions and effects not previously considered or thoroughly assessed. In particular, FTIR microspectroscopy and XRF highlighted that for higher doses an oxidation of both embedding medium and ultralene substrate takes place after the irradiated sample is exposed to air.

2. Materials and methods

2.1. Sample preparation

Four micrometre-thick slices of histological paraffin (Bio_Optica Milano SpA) were deposited onto a 4 µm-thick ultralene foil (SPEX SamplePrep) and onto 100 nm-thick Si_3N_4 membranes, both of them typical sample supports for soft X-ray microscopy analyses.

2.2. Soft X-ray exposure

Paraffin (deposited on ultralene or Si_3N_4 membranes), pristine ultralene foils and pristine Si_3N_4 membranes were exposed to different radiation doses in two different sessions at the TwinMic beamline (Gianoncelli *et al.*, 2016; Kaulich *et al.*, 2006) of Elettra-Sincrotrone Trieste (Trieste, Italy). The TwinMic microscope was operated in scanning mode, where the sample is raster-scanned across a monochromatic microprobe delivered by a zone plate diffractive optic. For the present experiment, an incident photon energy of 1.5 keV and a spot size of 1 µm diameter were used, representing typical experimental conditions for biological tissue analyses at TwinMic (Mitri *et al.*, 2017; Merolle, Sponder *et al.*, 2018; Pascolo *et al.*, 2018).

The different radiation doses (shown in Table 1) were delivered by adjusting the exposure time per pixel during the raster scan; samples were exposed to soft X-rays in two different sessions as explained in more detail in the following paragraphs. After each exposure, a fast STXM scan (delivering a further dose equal to Rad1) was performed in order to observe any immediate changes. For exposures longer than 1 s per pixel, XRF spectra were also simultaneously acquired. As described in the following paragraphs, the irradiation occurred in two steps: first, delivering doses from Rad1 to Rad5 (see Table 1); and second, after removing the sample from the vacuum, leaving it in ambient conditions and analyzing it with FTIR, delivering final doses from Rad1* to Rad5* (see Table 1). The X-ray transmission images acquired

Table 1
Delivered doses.

First session	Exposure time (ms)	Dose (Gy)	Second session	Exposure time (ms)	Dose (Gy)
Rad0	0	0	Rad0*	0	0
Rad1	20	1.28×10^6	Rad1*	40	2.56×10^6
Rad2	240	1.54×10^7	Rad2*	4100	2.63×10^8
Rad3	1060	6.81×10^7	Rad3*	5060	3.25×10^8
Rad4	5060	3.25×10^8	Rad4*	5120	3.29×10^8
Rad5	10060	6.46×10^8	Rad5*	10120	6.50×10^8

during exposures and presented in this work were normalized by the incident beam intensity in order to calculate the sample transmission. XRF oxygen chemical maps were analysed using the *PyMCA* software (Solé *et al.*, 2007).

2.3. FTIR microspectroscopy

Samples were inspected at the SISSI beamline (Lupi *et al.*, 2007) (Elettra–Sincrotrone Trieste, Trieste, Italy) with FTIR microspectroscopy using a Hyperion 3000 Vis–IR microscope coupled with a Bruker Vertex 70v interferometer equipped with a 64×64 pixels liquid-nitrogen-cooled bi-dimensional focal plane array (FPA) detector using a globar source. Paraffin (deposited on ultralene or Si_3N_4 membranes), pristine ultralene foils and Si_3N_4 membranes unexposed were first measured (Fig. 1). Then, after irradiation with specific delivered doses (Table 1), the X-ray exposed areas were identified and imaged again. For each sample, hyperspectral images were acquired in transmission mode using a $15\times$ condenser/objective, achieving a pixel size of $\sim$2.6 µm, generating each time an image of 4096 spectra by averaging 256 scans for each pixel with a spectral resolution of 4 cm^{-1}. Some images were acquired as a mosaic to cover larger areas (up to 2×2 tiles). Background images were acquired in air. All acquisitions were corrected for atmospheric water-vapour and CO_2 contributions with the routine of *OPUS* (version 7.5; Bruker Optics GmbH, Germany). Before hyperspectral analysis, data were baseline-corrected using *OPUS*. For ultralene, concave rubberband correction with 10 iterations and 25 baseline points was used. For paraffin on ultralene, concave rubberband correction with 3 iterations and 80 baseline points was used. Lastly, for paraffin on Si_3N_4, concave rubberband correction with 10 iterations and 25 baseline points was used.

Chemical images were generated by integrating the area under the curve for different spectral ranges. For instance, the integration of the asymmetric CH_3 band ($\sim$2960 cm^{-1}) for pristine ultralene and paraffin on ultralene samples or the CH_2 band (2850 cm^{-1}) for paraffin on Si_3N_4 membranes allowed us to highlight the different exposed areas. After the identification of the areas using this chemical image, average spectra for the different doses were extracted and used in the analysis; the edges of the regions were excluded in order to avoid artefacts.

To better highlight sample degradation, the second derivative of the spectra was calculated using the Savitzky–Golay filter with 9 smoothing points in the 3000–2800 infrared region.

For Fig. 4, integration of the FTIR spectra was performed as the area integral, using a linear baseline, of the following infrared regions: 1800–1520 cm^{-1} and 3730–3100 cm^{-1} (OH). All data were normalized to the maximum value of the dataset for each spectral range. This selection of infrared regions was intentionally chosen to better highlight the contribution of the aforementioned chemical moieties on different substrates.

3. Results and discussion

In the present work, we adopted the same approach used in the work by Bedolla *et al.* (2018), exposing the sample of interest to X-rays under vacuum, and then evaluating the extent of the radiation-induced changes through FTIR microspectroscopy in air.

As previously mentioned, this work is a further step to evaluate whether not only soft X-rays but also the subsequent exposure to air affects the chemical composition of both paraffin soft-tissue embedding medium and conventional soft X-ray substrates, and whether these effects change over time (ageing).

3.1. Zero-exposure condition

First of all, paraffin on ultralene, paraffin on Si_3N_4, ultralene and Si_3N_4 membranes were all characterized by FTIR microspectroscopy in their pristine state (no exposure to X-rays, Rad0 in Table 1). Fig. 1 shows the average infrared spectra in two spectral ranges: the first from 3050–2750 cm^{-1}, characteristic of stretching modes of aliphatic chains, and the second at lower energies 1500–900 cm^{-1} containing, among others, the bending signals of the aliphatic chains. The pristine Si_3N_4 was exposed to radiation and the FTIR average spectrum did not present spectral bands sensitive to X-ray exposure in the aforementioned regions (data not shown). For the samples considered in Fig. 1, several differences can be observed among the stretching signals regarding the methyl groups. Paraffin on an Si_3N_4 membrane (in blue) depicts the highest CH_2/CH_3 ratio, reflecting its chemical composition of long chains with no ramifications. On the contrary, as expected, ultralene (in red) has very intense methyl bands, since it is an isoprene-based polymer or a mixture of polypropylene and polyethylene as reported in the work by Ozzetti *et al.*
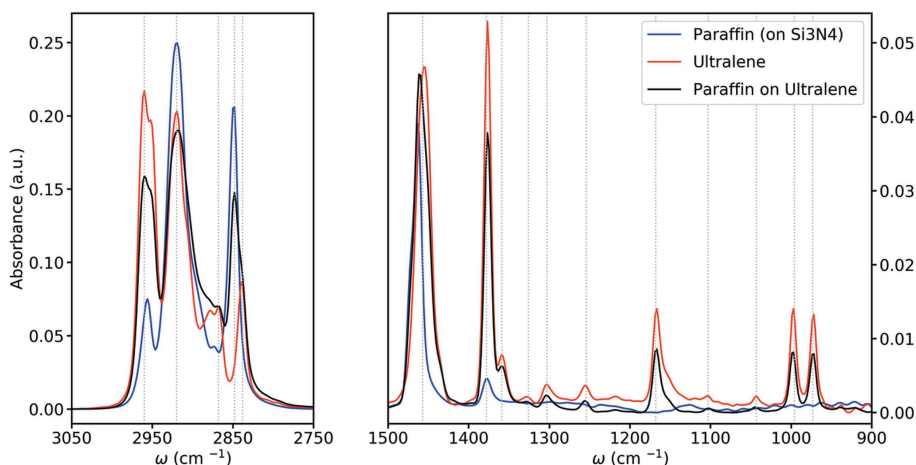

Figure 1
Reference FTIR spectra of paraffin on Si_3N_4 (blue), ultralene (red) and paraffin on ultralene (black). Vertical lines indicate the spectral frequencies: 2960, 2920, 2868, 2848, 2838, 2722, 1457, 1378, 1359, 1326, 1303, 1254, 1168, 1103, 1043, 996, 973 cm^{-1}.

Bedolla *et al.* · Oxidation due to radiation damage after exposure to soft X-rays

(2002). The difference in aliphatic chains between ultralene and paraffin can be distinguished by considering the bending modes: for ultralene both methyl and methylene are present at 1376 cm^{-1} and 1544 cm^{-1}, respectively, whereas the paraffin spectrum is dominated only by methylene bending at 1463 cm^{-1} (Ozzetti et al., 2002). The black FTIR spectrum was acquired on paraffin deposited on ultralene and therefore portraits all the aforementioned peaks. After this first characterization, the samples of interest were all exposed to a first session of soft X-ray irradiation.

3.2. First session of exposure

During this first session of exposure, the protocol shown in Fig. 2(a) was followed. The X-ray exposure was performed by scanning the sample and regulating the exposure time per pixel in order to deliver the desired dose. The doses are detailed in Table 1. In this session, a 240 μm × 160 μm region was firstly exposed to a small dose (Rad1) and then sub-regions were further exposed to four different increasing radiation doses (Rad2, Rad3, Rad4 and Rad5). After each exposure, a fast STXM scan (delivering a further dose equal to Rad1, see Table 1) was performed in order to evaluate possible mass loss and/or morphological changes. The right columns of Figs. 2(b)–2(d) show the absorption images acquired immediately after the exposure for the sample of interest, highlighting the effects of the irradiation. Inspection of the STXM images revealed that ultralene presents a higher

transmission in the exposed areas [Fig. 2(b)], outlined by a brighter square, which could indicate a temporary loss of material while the sample was still in the vacuum chamber. No visible changes related to the exposure were evident from the absorption images in the case of paraffin deposited on Si$_3$N$_4$ membranes [Fig. 2(c)]. On the other hand, in paraffin on the ultralene system [Fig. 2(d)], even if no significant transmission changes are detectable at lower doses; at the highest dose the sample becomes darker, indicating a lower transmission signal.

After these series of exposures, the samples were removed from the vacuum chamber of the TwinMic microscope and transferred to SISSI Beamline to perform FTIR micro-spectroscopy measurements in air at specific times: after an hour, a day and a week.

For the empty Si$_3$N$_4$ membrane and paraffin on Si$_3$N$_4$ cases, the measurements were performed after 6 h and after one week due to unavailability of the instrument.

3.3. Second session of exposure

The second session of soft X-ray irradiation, performed after the first session of FTIR measurements, consisted of additional irradiations of the already exposed areas one week after the first session. A wider area on the already highly exposed regions was further exposed to soft X-rays in order to increase the total dose, generating different areas to compare. The areas previously exposed to Rad3 and Rad4 doses and their surroundings were further irradiated with total new doses [see Figs. 2(e)–2(h)] Rad1*, Rad2*, Rad3*, Rad4* and Rad5* (see Table 1). After the second session of exposure, the samples appear overall more transparent to X-rays indicating a possible mass loss due to the first round of exposure. Note that all absorption images in Fig. 2 are intentionally plotted using the same intensity scale to allow for a direct comparison between the first and second sessions. Also, it is noticeable that after the samples have been exposed to air, the regions with the highest radiation become darker, which means a lower transmission signal. These dark regions are where the samples have been oxidized, as shown later on. To the naked eye, the exposed areas appear yellowish (data not shown). These observations are in agreement with what resulted from the FTIR measurements as will be shown in the following sections.

3.4. FTIR microspectroscopy results on exposed samples

In order to identify the exposed zones on the ultralene and paraffin on ultralene samples, chemical images were generated by integrating the band of the asymmetric stretch of CH$_3$ (2960 cm^{-1}), which has been proven to be sensitive to radiation (Bedolla et al., 2018). However, for the measurements of paraffin on Si$_3$N$_4$ membranes, the symmetric CH$_2$ band at 2850 cm^{-1} is the most sensitive. Spectra were extracted and averaged according to the dose and time.

In Fig. 3(a) the infrared spectra of paraffin on ultralene corresponding to Rad0* and Rad5* are presented as an example on the maximum difference observed. In order to evaluate the radiation-dependent degradation of the samples
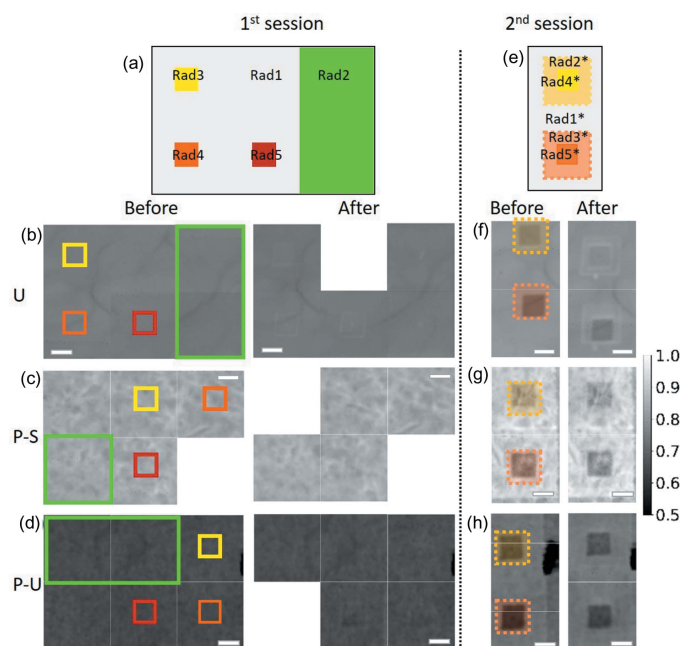

Figure 2
(a)–(d) First session of exposure and (e)–(h) second session of exposure. (a) and (e) Dose exposure protocol scheme; (b) and (f) ultralene substrate (U); (c) and (g) paraffin on Si$_3$N$_4$ (P-S); (d) and (h) paraffin on ultralene (P-U). For representation reasons, the corresponding exposed area for (c) is represented in (g) by rotating the images 90° clockwise. Panels (f), (g) and (h) (left column) are coloured in order to better highlight the exposed areas. The white scale bar represents 25 μm. The colour bar shows the transmission signal for all images.
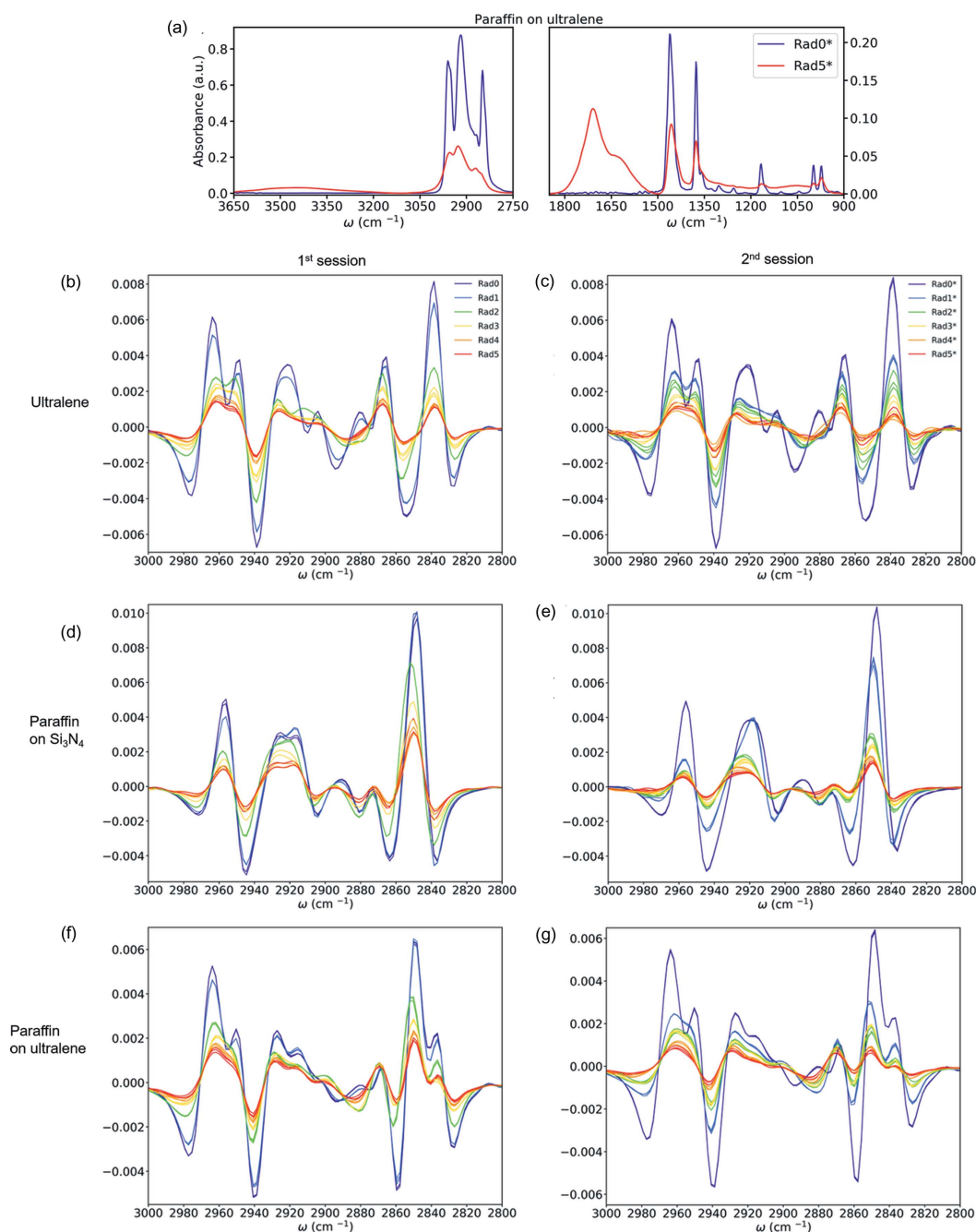
Figure 3
(*a*) Absorbance spectra of paraffin on ultralene at Rad0* and Rad5*. Second derivative of the FTIR spectra in the 3650–2800 cm^{-1} region of the (*b*), (*d*), (*f*) first and (*c*), (*e*), (*g*) second session of exposure. Each colour represents a radiation level. Different air exposure times (1 h, 1 day, 1 week) are represented by the corresponding radiation colours (violet Rad0–Rad0*; blue Rad1–Rad1*; green Rad2–Rad2*; yellow Rad3–Rad3*; orange Rad4–Rad4*; red Rad5–Rad5*).

of interest, in Figs. 3(*b*)–3(*g*), the second derivative of the three systems studied in the 3000–2800 cm^{-1} region is presented for the first [Figs. 3(*b*), 3(*d*) and 3(*f*)] and second [Figs. 3(*c*), 3(*e*) and 3(*g*)] exposure sessions. Each colour represents a radiation level. Different air-exposure times are represented all with the same colour (*i.e.* Rad1 1 h, 1 day or 1 week are blue). The overlapping of the curves with the same colour actually implies no significant change due to the different air exposure times for the considered infrared region.

Furthermore, the degradation of the materials is evident by the loss of sharpness in the peaks when the radiation dose increases. In the absorbance data, an overall depletion of the intensity of the inspected bands was observed [see Fig. 3(*a*) as an example]. Therefore, a decrease in the quantity of the observed chemical moieties upon irradiation is indicated, specifically of the C—H single bond, as has already been observed and presented in the work by Bedolla *et al.* (2018). In the first session, there is an obvious degradation happening

already after the delivery of Rad1 dose on ultralene [Fig. 3(b)], yet the change is more noticeable after Rad2 for the paraffin samples. On the other hand, for the second session, all systems show a substantial degradation after Rad1. This indicates that the sample has a higher predisposition to change structure due to radiation. It is also interesting to note that while ultralene seems to gradually change by each step of radiation, for paraffin on Si_3N_4 it appears to happen as a two-step process, and for paraffin on ultralene as one-step jump from Rad2 on. The ultralene band at 2956 cm^{-1}, corresponding to the asymmetric stretching of CH_3, is more prone to damage at higher doses as its derivative greatly changes with increasing doses. This is not surprising since ultralene is polypropylene based thus it contains many CH_3 terminal branches.

Similar conclusions can be drawn from the bending signals at lower energies (1500–1400 cm^{-1}), although these signals have a lower intensity and a tighter overlapping so variations are less resolved (data not shown).

Upon exposure, it has been observed that the long aliphatic chains break. This leads to the generation of radicals that can diffuse into the film, further damaging the intact polymeric chains. Chain rupture can also generate dangling bonds that can be subsequently oxidized when exposed to air. This process is better shown in Fig. 4 where the normalized integration values for the 1800–1520 cm^{-1} and OH infrared regions are presented. The values are displayed in two different colours, corresponding to the two different exposure sessions, with tonalities of the same colour getting darker with increasing exposure time to air (1 h, 24 h, 1 week). In particular, Figs. 4(a), 4(c) and 4(e) show the evolution of the 1800–1520 cm^{-1} region in the three analysed samples. This signal is the convolution of two main bands, centred at 1709 cm^{-1} and 1620 cm^{-1}. For all the systems the trend is similar: it increases with time and dose. Note that the physical phenomena represented by these signals show two steps. After the first session, there are some detectable signals but only at higher
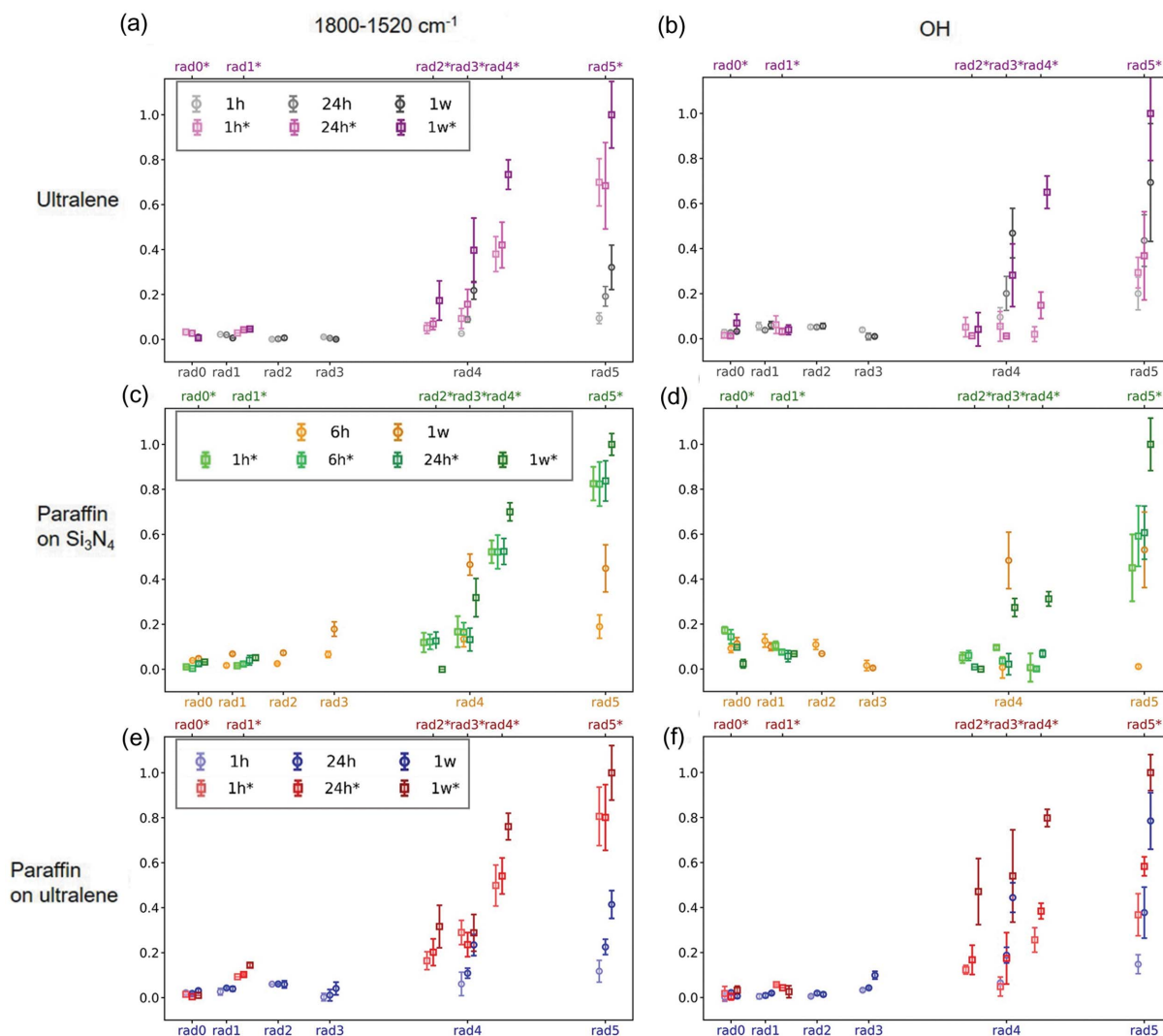

Figure 4
Scatter plots of the normalized integration values of bands of interest in the FTIR spectra. The abscissa represents the state of radiation, the axis on the bottom represents the values of the first session, and those above are the values of the second session denoted by the name and asterisk (i.e. Rad1*). Time between breaking the vacuum and the FTIR measurement is shown by the change from light (from 1 h) to dark colour (up to 1 week). For clarity, distances between ticks on the x axis are not directly proportional to the radiation values.

doses, whereas for the second session, the 1800–1520 cm^{-1} region shows more pronounced changes for all acquisition times (1 h, 24 h, 1 week). The most evident dose case is at Rad5–Rad5*, where both first and second sessions show a significant difference between the three time points (1 h, 24 h and 1 week) for ultralene and paraffin on ultralene [Figs. 4(a) and 4(e)], as well as for the two time points (6 h, 1 week) for paraffin on Si$_3$N$_4$ [Fig. 4(c)], though less pronounced for the second session. A similar behaviour is observed when looking at the broad band around 3460 cm^{-1} [Figs. 4(b), 4(d) and 4(f)] corresponding to the stretching of OH, where a clear increase is observed after a period of time exposed to air. In particular, these differences are more evident after Rad4 of the first exposure, or after Rad3* of the second.

In fact, some of the infrared bands detected by other authors as indicative of an oxidation process are also noticeable in this work. The appearance of C=O, seen around 1709 cm^{-1}, can be related to the development of different carbonyl-containing groups (Salimi *et al.*, 2009) such as ketones, aldehydes, esters and carboxylic acids. Instead, the observed contribution around 1620 cm^{-1} has previously been attributed to double-bond stretching (Lazár *et al.*, 2000) which might be explained by fragmentation into shorter chains, sometimes generating allyl or polyenyl radical species (Bertin *et al.*, 2010; Williams, 1991). This raise could be linked to the incorporation of water as well, attributing the increase of the 1620 cm^{-1} peak to the OH bending signal. As a matter of fact, it is known that oxidized polymers can be converted into more hydrophilic fragments (Kornacka, 2017). This is supported by the contemporary increase of the broad infrared band at 3250–3600 cm^{-1}, attributed to stretching of the hydroxyl groups. Furthermore, it has been reported that hydroperoxide formation may be detected in this spectral region (3410 cm^{-1}

and 3550 cm^{-1}), appearing before the generation of a variety of carbonyl and hydroxyl groups that may further propagate by hydroperoxide decomposition into alkoxy- and preoxy-type radicals (Salimi *et al.*, 2009).

All these observations are also confirmed by comparing the low-energy XRF oxygen maps acquired during both sessions. Fig. 5 displays the oxygen maps for the three samples of interest for both sessions of exposure. After the first XRF maps and the subsequent specimen's exposure to air, the area exposed to dose Rad3 and Rad4 showed a dramatic increase in oxygen [column '2nd session': Figs. 5(b), 5(d), 5(f), 5(h), 5(j) and 5(l)]. The map collected during the first session shows no oxygen (very low counts) for all the sample typologies: this is expected since none of the exposed materials contain oxygen. This is due to the fact that they are collected simultaneously to the irradiation and so the overall effect will be visible only with a second acquisition; however, since the XRF maps in Figs. 5(g), 5(i) and 5(k) were acquired with a longer exposure time, compared with Figs. 5(a), 5(c) and 5(e), a slight increase in the oxygen counts is observed. After exposure to air, the maps acquired during the second session, which contain the maps acquired in the first session, clearly show the presence of oxygen. This supports the hypothesis of an oxidation process caused by exposure to air when paraffin and ultralene are exposed to high doses. Although for the Rad3 dose [regions surrounding the areas mapped with 1 s per pixel of exposure time in Figs. 5(b), 5(d) and 5(f)] there is no substantial oxygen increase after air exposure for paraffin on Si$_3$N$_4$, for ultralene and paraffin on ultralene there is an increase. However, such an oxygen count increase is much lower than what was detected for Rad4 [areas mapped with 5 s per pixel in the first session, corresponding to Figs. 5(h), 5(j) and 5(l)].
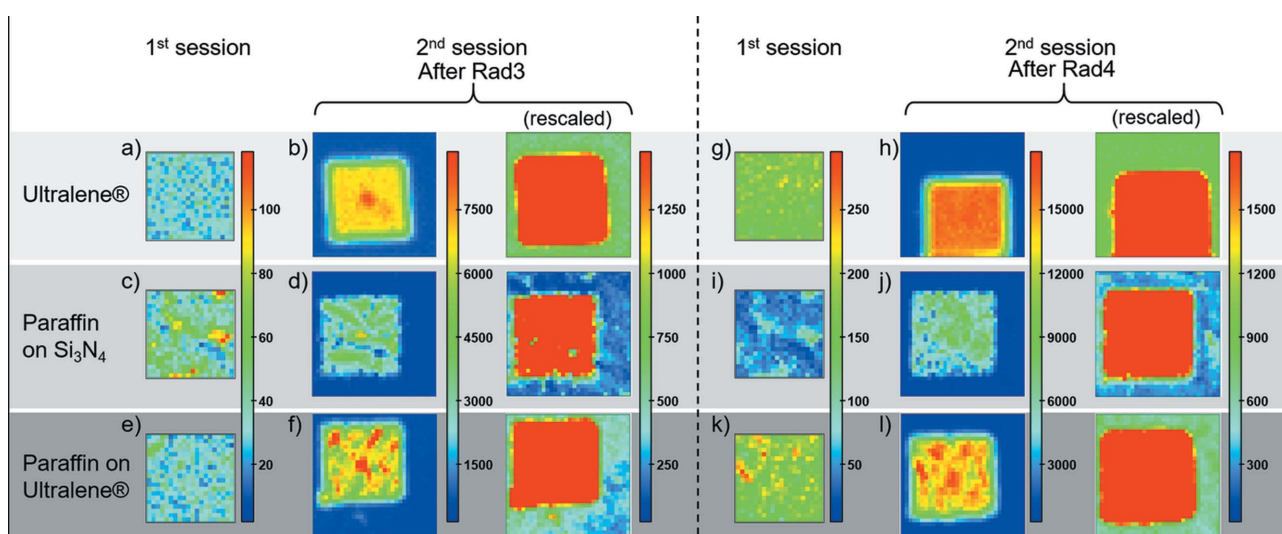

Figure 5
Oxygen X-ray fluorescence maps on (a), (b), (g), (h) ultralene, (c), (d), (i), (j) paraffin on Si$_3$N$_4$ membranes and (e), (f), (k), (l) paraffin on ultralene. In the first session (a), (c), (e) an area previously exposed to Rad3 and (g), (i), (k) another area to Rad4. After breaking the vacuum, a bigger area which covered the area already exposed in the first session was further exposed to observe the effect of the first session, delivering a final dose corresponding to (b), (d), (f) Rad3* or (h), (j), (l) Rad5*. These last panels present the same O map with two different scales to better highlight the intensity values inside the twice-exposed (central panel) and the single-exposed area (surrounding area).

3.5. Summary

Considering all the data, we can speculate more about the chemical changes happening within the inspected films during and after the irradiation processes.

From the literature, it is shown that ultralene is a polymer similar to polyethylene/polypropylene (Ozzetti *et al.*, 2002), and several authors have already reported that polyethylene/polypropylene is prone to degradation (Salimi *et al.*, 2009; Shibryaeva *et al.*, 2010; Cai *et al.*, 2009). Blakey and authors observed that polypropylene, upon thermal exposure at 150°C, oxidized under an oxygen atmosphere (Blakey & George, 2001). In addition, Heude *et al.* studied the oxidation of polypropylene under UV exposure (François-Heude *et al.*, 2015), Bertin *et al.* by increasing the temperature of exposure (Bertin *et al.*, 2010), and Blakey *et al.*, Lacoste *et al.* and Tidjiani *et al.* with gamma-, photo- and thermally initiated oxidation (Blakey & George, 2001; Lacoste & Carlsson, 1992; Tidjani & Watanabe, 1996). In all these studies, oxidation was observed as a response to an activation process due to thermal exposure, instead ours focuses on the effect of multiple soft X-ray irradiations and oxidation at ambient conditions.

In the current study, we observed that after samples were exposed to air and received a dose larger than Rad2*, the damaging process was not only dose-dependent, as is the case for the aliphatic chain signal trend, but also time-dependent when exposed to air. In light of these observations, a multi-step process can be hypothesized: X-ray exposure first causes a scission of the C—C and C—H bonds of the polymers, and the subsequent exposure to air causes a mild oxidation/absorption of water. At lower doses the phenomenon affects the most superficial layers, so it is not clearly detectable, though it becomes more evident at higher doses being the effects greater. The second session of exposure also affects the less exposed areas, which already contain some water/oxygen, generating more initiation points that propagate through to the polymeric film, causing scissions and further oxidation after coming into contact with air again. For doses larger than Rad2*, the oxidation process continues with time, even after a week there is no clear formation of a plateau. To summarize, we believe that the oxidation is promoted by radicals formed in the irradiated film that further react with the environmental oxygen and water. The velocity of oxidation is limited by the permeability of the oxygen in the film and the diffusion of radicals. This explains why the process starts slowly at low doses. Then, when the radiation dose produces a sufficient number of radicals and broken bonds, the reaction accelerates and the oxygen level increases. This process was further confirmed by the XRF maps of oxygen (Fig. 5) and from the absorption images (Fig. 2) acquired before and after irradiation and before and after exposure to air. It appears that when still in the vacuum chambers, the highest irradiation doses cause a temporary mass loss in the exposed material – polymeric chain breaking – whereas after exposure to air, the material appears darker, less transparent, which indicates a denser state, further supporting the hypothesis of an oxidation process happening in response to air exposure.

4. Conclusions

In this work, three different types of samples were tested: ultralene, paraffin on Si_3N_4 membranes and paraffin on ultralene. We confirmed that in the polymeric films the generation of radicals and dangling bonds requires a certain energy delivery (up to Rad2); before that, only a decrease in chain length can be observed from an aliphatic point of view and no detectable oxidation process is reflected. When this threshold is surpassed, the oxidation proceeds more rapidly and the number of oxidized species increases in time, even without further exposure. This result is further supported by the XRF maps obtained from the sample, where the increase in oxygen concentration after air exposure is quite evident. It is important to stress from our results that, when performing XRF microscopy on light elements, if the maps are repeated after a first high-dose exposure followed by exposure to air, the oxygen levels may appear different in the following XRF maps, due to the identified oxidation process. Therefore, mapping the same area twice might not be desirable. This implies that if the analysed samples already contain oxygen or easily ionizing chemicals, X-ray microscopists should then carefully consider this effect. In particular, when performing quantitative evaluations of light element concentrations, one should properly plan sample preparation and measurements. As it is known, quantification of light elements is already difficult due to self-absorption effects in the samples and the unavailability of certified reference standards. Also, substrates that were thought to be unaffected by radiation when interacting with biological matter showed radiation damage (Surowka *et al.*, 2020). On the contrary, other materials like paraffin that are more prone to be affected by radiation may show more resilience by dispersing the energy through melting or softening instead of modifying the biological sample (Surowka *et al.*, 2020). The current work demonstrates that radiation damage is a further factor, sometimes not negligible, which can affect the quantification results if not properly evaluated and considered. Moreover, with the advent of new diffraction limited storage rings, the issue of radiation damage will become greater, especially for sensitive samples like biological ones, principally for micro- or nano-focus beam-lines.

References

Bedolla, D. E., Mantuano, A., Pickler, A., Mota, C. L., Braz, D., Salata, C., Almeida, C. E., Birarda, G., Vaccari, L., Barroso, R. C. & Gianoncelli, A. (2018). *J. Synchrotron Rad.* **25**, 848–856.
Beetz, T. & Jacobsen, C. (2003). *J. Synchrotron Rad.* **10**, 280–283.
Bertin, D., Leblanc, M., Marque, S. R. A. & Siri, D. (2010). *Polym. Degrad. Stabil.* **95**, 782–791.
Blakey, I. & George, G. A. (2001). *Macromolecules*, **34**, 1873–1880.

Cai, Y., Wei, Q., Huang, F., Lin, S., Chen, F. & Gao, W. (2009). *Renew. Energy*, **34**, 2117–2123.

Carugo, O. & Djinović Carugo, K. (2005). *Trends Biochem. Sci.* **30**, 213–219.

Chwiej, J., Szczerbowska-Boruchowska, M., Lankosz, M., Wojcik, S., Falkenberg, G., Stegowski, Z. & Setkowicz, Z. (2005). *At. Spectrosc.* **60**, 1531–1537.

François-Heude, A., Richaud, E., Desnoux, E. & Colin, X. (2015). *J. Photochem. Photobiol. Chem.* **296**, 48–65.

Gianoncelli, A., Kourousias, G., Merolle, L., Altissimo, M. & Bianco, A. (2016). *J. Synchrotron Rad.* **23**, 1526–1537.

Gianoncelli, A., Vaccari, L., Kourousias, G., Cassese, D., Bedolla, D. E., Kenig, S., Storici, P., Lazzarino, M. & Kiskinova, M. (2015). *Sci. Rep.* **5**, 10250.

Howells, M. R., Beetz, T., Chapman, H. N., Cui, C., Holton, J. M., Jacobsen, C. J., Kirz, J., Lima, E., Marchesini, S., Miao, H., Sayre, D., Shapiro, D. A., Spence, J. C. H. & Starodub, D. (2009). *J. Electron Spectrosc. Relat. Phenom.* **170**, 4–12.

Jones, M. W. M., Hare, D. J., James, S. A., de Jonge, M. D. & McColl, G. (2017). *Anal. Chem.* **89**, 12168–12175.

Jones, M. W. M., Kopittke, P. M., Casey, L., Reinhardt, J., Blamey, F. P. C. & van der Ent, A. (2020). *Ann. Bot.* **125**, 599–610.

Kaulich, B., Bacescu, D., Susini, J., David, C., Di Fabrizio, E., Morrison, G. R., Charalambous, P., Thieme, J., Wilhein, T., Kovac, J., Cocco, D., Salomé, M., Dhez, O., Weitkamp, T., Cabrini, S., Cojoc, D., Gianoncelli, A., Vogt, U., Podnar, M., Zangrando, M., Zacchigna, M. & Kiskinova, M. (2006). *Conf. Proc. Ser. IPAP*, **7**, 22–25.

Kornacka, E. M. (2017). *Applications of Ionizing Radiation in Materials Processing*, Vol. 1. Warsaw: Institute of Nuclear Chemistry and Technology.

Kosior, E., Cloetens, P., Devès, G., Ortega, R. & Bohic, S. (2012). *Appl. Phys. Lett.* **101**, 263102.

Lacoste, J. & Carlsson, D. J. (1992). *J. Polym. Sci. A Polym. Chem.* **30**, 493–500.

Lazár, M., Hřcková, L., Borsig, E., Marciňcin, A., Reichelt, N. & Rätzsch, M. (2000). *J. Appl. Polym. Sci.* **78**, 886–893.

Lombi, E., de Jonge, M. D., Donner, E., Kopittke, P. M., Howard, D. L., Kirkham, R., Ryan, C. G. & Paterson, D. (2011). *PLoS One*, **6**, e20626.

Lupi, S., Nucara, A., Perucchi, A., Calvani, P., Ortolani, M., Quaroni, L. & Kiskinova, M. (2007). *J. Opt. Soc. Am. B*, **24**, 959–964.

Merolle, L., Ragazzi, M., Gianoncelli, A., Altissimo, M., Ciarrocchi, A., Bedolla, D. E., Marraccini, C., Baricchi, R. & Pertinhez, T. A. (2018). *J. Inst.* **13**, C05018.

Merolle, L., Sponder, G., Sargenti, A., Mastrototaro, L., Cappadone, C., Farruggia, G., Procopio, A., Malucelli, E., Parisse, P., Gianoncelli, A., Aschenbach, J. R., Kolisek, M. & Iotti, S. (2018). *Metallomics*, **10**, 917–928.

Mitri, E., Millucci, L., Merolle, L., Bernardini, G., Vaccari, L., Gianoncelli, A. & Santucci, A. (2017). *Biochim. Biophys. Acta*, **1861**, 1000–1008.

Ozzetti, R. A., De Oliveira Filho, A. P., Schuchardt, U. & Mandelli, D. (2002). *J. Appl. Polym. Sci.* **85**, 734–745.

Pascolo, L., Gianoncelli, A., Schneider, G., Salomé, M., Schneider, M., Calligaro, C., Kiskinova, M., Melato, M. & Rizzardi, C. (2013). *Sci. Rep.* **3**, 1123.

Pascolo, L., Venturin, I., Gianoncelli, A., Bortul, R., Zito, G., Giolo, E., Salomé, M., Bedolla, D. E., Altissimo, M., Zweyer, M. & Ricci, G. (2018). *Reprod. Biomed. Online*, **37**, 153–162.

Paunesku, T., Wanzer, M. B., Kirillova, E. N., Muksinova, K. N., Revina, V. S., Lyubchansky, E. R., Grosche, B., Birschwilks, M., Vogt, S., Finney, L. & Woloschak, G. E. (2012). *Health Phys.* **103**, 181–186.

Pickler, A., Mantuano, A., Mota, C. L., Ferreira-Machado, S., Lau, C. C., de Almeida, C. E., Salata, C., Nascimento, A., Tanure, T., Serqueira, L., Sena, G., Fidalgo, G., Colaço, M., Bedolla, D., Gianoncelli, A., Braz, D. & Barroso, R. C. (2019). *Microchem. J.* **148**, 467–474.

Salimi, A., Atai, M., Mirabedini, M. & Mohseni, M. (2009). *J. Appl. Polym. Sci.* **111**, 2703–2710.

Sanishvili, R., Yoder, D. W., Pothineni, S. B., Rosenbaum, G., Xu, S., Vogt, S., Stepanov, S., Makarov, O. A., Corcoran, S., Benn, R., Nagarajan, V., Smith, J. L. & Fischetti, R. F. (2011). *Proc. Natl Acad. Sci. USA*, **108**, 6127–6132.

Shibryaeva, L. S., Shatalova, O. V., Solovova, Yu. V., Korzh, N. N. & Krivandin, A. V. (2010). *Theor. Found. Chem. Eng.* **44**, 436–447.

Solé, V. A., Papillon, E., Cotte, M., Walter, P. & Susini, J. (2007). *At. Spectrochim. Acta Part B At. Spectrosc.* **62**, 63–68.

Surowka, A. D., Gianoncelli, A., Birarda, G., Sala, S., Cefarin, N., Matruglio, A., Szczerbowska-Boruchowska, M., Ziomber-Lisiak, A. & Vaccari, L. (2020). *J. Synchrotron Rad.* **27**, 1218–1226.

Takahashi, M., Kinoshita, H., Nishiguchi, M. & Nishio, H. (2010). *Leg. Med.* **12**, 102–103.

Tidjani, A. & Watanabe, Y. (1996). *J. Appl. Polym. Sci.* **60**, 1839–1845.

Wang, J., Morin, C., Li, L., Hitchcock, A. P., Scholl, A. & Doran, A. (2009). *J. Electron Spectrosc. Relat. Phenom.* **170**, 25–36.

Williams, J. L. (1991). *ACS Symp. Ser.* **475**, 554–568.